Lab on a Chip

Cite this: *Lab Chip*, 2012, **12**, 731

www.rsc.org/loc

PAPER

A silicone-based stretchable micropost array membrane for monitoring live-cell subcellular cytoskeletal response†

Jennifer M. Mann,‡[ab] Raymond H. W. Lam,§‡[ab] Shinuo Weng,[ab] Yubing Sun[ab] and Jianping Fu*[abc]

Received 17th September 2011, Accepted 8th December 2011
DOI: 10.1039/c2lc20896b

External forces are increasingly recognized as major regulators of cellular structure and function, yet the underlying mechanism by which cells sense forces and transduce them into intracellular biochemical signals and behavioral responses ('mechanotransduction') is largely undetermined. To aid in the mechanistic study of mechanotransduction, herein we devised a cell stretching device that allowed for quantitative control and real-time measurement of mechanical stimuli and cellular biomechanical responses. Our strategy involved a microfabricated array of silicone elastomeric microposts integrated onto a stretchable elastomeric membrane. Using a computer-controlled vacuum, this micropost array membrane (mPAM) was activated to apply equibiaxial cell stretching forces to adherent cells attached to the microposts. Using the mPAM, we studied the live-cell subcellular dynamic responses of contractile forces in vascular smooth muscle cells (VSMCs) to a sustained static equibiaxial cell stretch. Our data showed that in response to a sustained cell stretch, VSMCs regulated their cytoskeletal (CSK) contractility in a biphasic manner: they first acutely enhanced their contraction to resist rapid cell deformation ('stiffening') before they allowed slow adaptive inelastic CSK reorganization to release their contractility ('softening'). The contractile response across entire single VSMCs was spatially inhomogeneous and force-dependent. Our mPAM device and live-cell subcellular contractile measurements will help elucidate the mechanotransductive system in VSMCs and thus contribute to our understanding of pressure-induced vascular disease processes.

Introduction

Mechanotransduction is recognized as an essential physiological process through which cells interpret mechanical signals, such as applied forces or the rigidity of the extracellular matrix (ECM), from the surrounding cellular microenvironment and convert them into biochemically relevant information.[1–5] These subsequently regulate essential cellular functions including morphology, proliferation, migration, and stem cell differentiation.[6–11] Although applying forces to cells and altering the rigidity of their environment are clearly distinct processes, the underlying mechanisms of mechanotransduction seem to be similar and involve the modulation of intracellular cytoskeletal (CSK) contractility.[5,12,13] For example, cells plated on soft substrates exert lower contractile forces than cells plated on stiff ones, decreasing tensional stresses on force-bearing intracellular structural elements.[10,14,15] These elements are the same whether forces are generated internally or externally; thus, many of the cellular responses to distinct mechanical stimuli are similar. The similarities in cellular responses to perturbations in matrix rigidity and externally applied forces have led to the suggestion that both types of mechanical signals may use shared mechanotransduction pathways involving the CSK contractility to convert mechanical stimuli through the focal adhesion (FA) signaling apparatus into biochemical signals.[5,13]

Numerous developmental, physiological and pathological processes are influenced by mechanotransduction. For example, in the vasculature, hypertension increases circumferential tension and the degree of stretch in blood vessel walls. This causes smooth muscle and endothelial cell dysfunction, leading to hypertrophy and fibrosis in the vessel walls that in turn drive progression of the disease.[16–18] Thus, there is a great current interest in understanding mechanotransduction in vascular smooth muscle cells (VSMCs), or more specifically, the intimate interaction between externally applied forces (*i.e.*, cell stretching forces) and changes in CSK contractility of VSMCs, in the hope that better understanding will ultimately pave the way to

[a]*Integrated Biosystems and Biomechanics Laboratory, University of Michigan, Ann Arbor, MI, 48105, USA*
[b]*Department of Mechanical Engineering, University of Michigan, Ann Arbor, MI, 48105, USA*
[c]*Department of Biomedical Engineering, University of Michigan, Ann Arbor, MI, 48105, USA. E-mail: jpfu@umich.edu; Fax: +01-734-647-7303; Tel: +01-734-615-7363*

† Electronic supplementary information (ESI) available. See DOI: 10.1039/c2lc20896b

‡ These authors contributed equally to this work.

§ Current address: Department of Mechanical and Biomedical Engineering, City University of Hong Kong, Hong Kong.

developing drugs that specifically interfere with pressure-induced vascular pathologies. Indeed, CSK contraction in VSMCs plays an important functional role in regulating adaptation and remodeling of vessel walls in hypertension, which can subsequently lead to fatal human health problems such as stroke and other cardiovascular diseases.[19–21] Further, stretch-mediated VSMC contractile behavior is a key mechanism for the establishment of myogenic tone and the auto-regulation of blood flow and pressure.[22,23]

Force-mediated contractile phenotypic change in VSMCs is critically involved in the progression of hypertension-induced vascular pathologies. Yet, there is still very limited understanding of the early mechanotransduction process in VSMCs that results in their acute biomechanical responses such as their contractility modulation. This limited knowledge of the contractile phenotypic change in VSMCs is at least partially due to the fact that very few tools currently exist to precisely modulate external mechanical forces while simultaneously quantifying live-cell CSK contractility responses. A number of techniques are currently in use for the application of well-controlled forces at the cellular and subcellular levels.[24–27] Broadly speaking, these techniques fall into two classes: direct methods such as substrate deformation,[28–32] micropipette aspiration,[33,34] cell poking,[35] cell compression,[36] and atomic force microscopy,[37,38] where the force generation apparatus comes into direct contact with the cell, and indirect methods where the force is provided by the action of an optical or magnetic field on a functionalized micrometer-sized bead or magnetic silicone micropost bound to the cell surface.[39–49] Direct methods can generate a large global cell strain. Yet, it is difficult to determine the spatiotemporal responses of subcellular contractile forces and further attribute them directly to dynamically-regulated individual FAs. Indirect techniques are more compatible with optical microscopy, and thus it is possible to simultaneously exert forces on the bead or micropost and observe their responses to quantify the reactionary contractile forces. It remains largely unclear, however, whether the activation of CSK contractility by locally applied forces is spatially restricted to the subcellular region that experiences the force, or results in a global change in cellular mechanics. The indirect methods also suffer from variability among the data from different studies, which is suspected to be due to the regional heterogeneity and dynamic regulation of the cytoplasm and adhesions of cells.[50]

To aid in the mechanistic investigation of stretch-mediated VSMC contractile phenotypic change, herein we report a strategy to apply external homogeneous cell stretching forces and simultaneously monitor contractile responses of VSMCs by using a microfabricated array of silicone elastomeric posts attached to a stretchable elastomeric membrane. More specifically, our microengineered setup consisted of a cell stretching device (CSD) and a stretchable micropost array membrane (mPAM). The mPAM was a thin, 100 mm-diameter poly-(dimethylsiloxane) (PDMS) membrane with a square-shaped array of hexagonally spaced PDMS microposts formed at the membrane center (Fig. 1). The PDMS micropost array was first fabricated using microfabrication and replica molding on a thin layer of PDMS before it was bonded permanently onto the 100 mm-diameter thin PDMS base membrane, using the oxygen plasma-assisted PDMS-PDMS bonding process (see **Materials and Methods** for the mPAM fabrication method). The nominal spring constant K of a PDMS micropost is solely determined by its geometry and by the *Young*'s modules E of PDMS, and K can be approximately calculated using the *Euler-Bernoulli* beam theory as $K = 3\pi ED^4/(64L^3)$,[51–53] where D and L are the diameter and height of the PDMS micropost, respectively. Thus, the spring constant K can be modulated simply by varying the post height L while keeping all other aspects of the substrate such as the micropost diameter, surface chemistry, and ligand density unchanged.[15,54] The PDMS micropost array on the mPAM examined in this work had a post diameter D of 1.83 μm, a post center-to-center (c.t.c.) distance S of 4 μm, and post height L ranging from 0.97 μm to 14.7 μm.

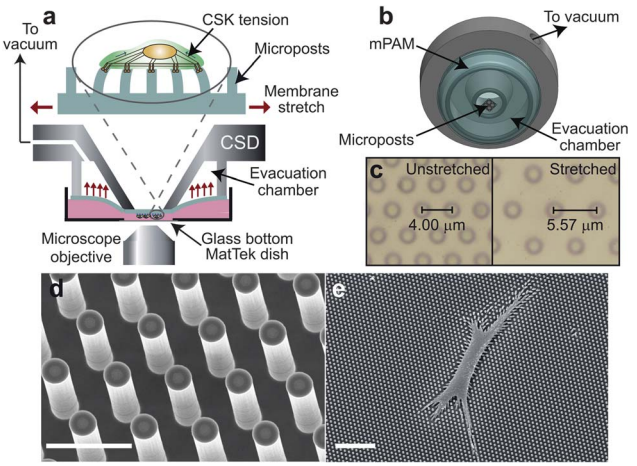

Fig. 1 A custom-designed cell stretching device (CSD) containing an elastomeric PDMS micropost array membrane (mPAM) to modulate equibiaxial cell stretch while simultaneously measuring real-time live-cell subcellular contractile response. (**a**) Schematic of the CSD (*gray*) with the mPAM (*blue*) affixed and single live cells attached on the mPAM (*green*, in a pink cell medium). A vacuum could be drawn in the evacuation chamber which the PDMS base membrane was pulled into, thus evenly stretching the PDMS micropost array over the viewing aperture. The real-time mPAM stretching process and live-cell subcellular contractile response were observed through the glass bottom of the MatTek dish. (**b**) Three-dimensional view of the CSD. Note the square shaped PDMS micropost array was centered over the viewing aperture. (**c**) Bright-field images of unstretched (*left*) and equibiaxially stretched (*right*, 40%) PDMS micropost arrays. Note that the PDMS microposts were hexagonally spaced with the post c.t.c. distance increasing due to the mPAM stretch while the top surface of the PDMS microposts remained constant during the mPAM stretch. (**d**) Scanning electron microscopy (SEM) image of the PDMS microposts. Scale bar, 5 μm. (**e**) SEM of a single adherent cell attaching on the PDMS micropost tops. Note displacements of the micropost tops due to cellular contractile forces. Scale bar, 40 μm.

Results and discussion

The CSD was designed with a circular viewing aperture surrounded by a vacuum chamber, with the mPAM attached to the CSD and the PDMS micropost array centered on the viewing aperture to permit visualization of the microposts under an optical microscope (Fig. 1). The CSD was activated for cell stretch by applying a computer-controlled vacuum to draw the periphery of the PDMS base membrane into the vacuum

chamber, causing the central area of the mPAM holding the PDMS micropost array to stretch equibiaxially. The stretch magnitude of the mPAM was easily determined *in situ* by utilizing the regularly positioned PDMS microposts as fiduciary markers to quantify their increased c.t.c distance S under different levels of stretch. To confirm that stretch of the mPAM was indeed equibiaxial and spatially homogeneous over the entire PDMS micropost array, we applied different levels of static stretch to the mPAM with the stretch magnitude ranging from 0% to 20%. Both brightfield and fluorescence images were taken at the top surface of the PDMS microposts, which were labeled with the fluorescent dye DiI, at five different locations covering the entire micropost array through symmetry (Fig. 1c and Fig. 2a). Using the image processing program ImageJ, fluorescence images were analyzed to determine the increased post c.t.c. distance S (Fig. 2b) and the micropost diameter D (Fig. 2c) at each of these five locations. S varied by less than 2% among the 5 different locations, regardless of the stretch magnitude, suggesting that the mPAM stretch produced by the CSD was indeed homogeneous and equibiaxial over the entire micropost array (Fig. 2b). Similarly, regardless of the stretch magnitude, the diameter D of the top surface of the PDMS micropost, measured at the five different locations, remained constant, indicating that the mechanical strain generated within the PDMS base membrane during the mPAM stretch did not propagate up the micropost to change the micropost geometry (Fig. 2c). We further examined reliability of the mPAM under static stretch conditions. Our data in Fig. 2d confirmed that the mPAM could withstand a constant static stretch for at least 1 h under a broad range of stretch magnitudes from 0% up to 20%.

To confirm that stretch of the mPAM would not affect the nominal spring constant K of the PDMS micropost (and thus the micropost rigidity perceived by adherent cells), we used the commercially-available finite element analysis (FEA) suite COMSOL to analyze defections of the PDMS microposts under horizontal traction forces for both unstretched and stretched conditions (Fig. 3). Our FEM model consisted of a cylindrical PDMS micropost (with the post height L of 0.97–12.9 μm) centered on the top surface of a 5 × 5 × 10 μm rectangular PDMS prism. The whole PDMS assembly was modeled as Neo-Hookian hyperelastic with a *Young*'s modulus E of 2.5 MPa, and was discretized into fine tetrahedral mesh elements calibrated for general physics in COMSOL. For unstretched mPAMs, the bottom and four sides of the rectangular PDMS prism were assigned fixed boundary conditions, while for stretched mPAMs, the bottom of the PDMS prism was constrained and the four side faces were prescribed a displacement that would reproduce a 25% stretch for the PDMS base membrane (as a worst-case-scenario of the mPAM stretch). Fig. 3a depicts the volumetric strain of the

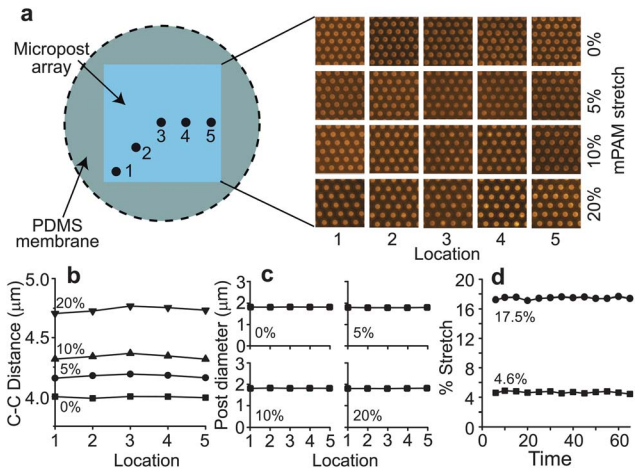

Fig. 2 Experimental characterization of the equibiaxial mPAM stretch using the CSD. (**a**) Five different locations evenly distributed across the PDMS micropost array (*blue*) were chosen for characterizing the equibiaxial mPAM stretch. The PDMS microposts were stained with DiI for visualization. The vacuum was modulated to apply 0%, 5%, 10%, and 20% static equibiaxial mPAM stretches. (**b**) Center-to-center (c.t.c.) distances of adjacent PDMS microposts under 0% (■), 5% (●), 10% (▲), and 20% (▼) static mPAM stretches at the five different locations as indicated in **a**. (**c**) Diameters of the PDMS micropost tops measured from the fluorescence images shown in **a**, with the mPAM equibiaxially stretched under different stretch magnitudes as indicated. (**d**) Reliability test of the mPAM showing that under constant vacuum, stable static mPAM stretch (with the stretch magnitude ranging from 0% to 20%) was achieved over a time period of at least 1 h, with the c.t.c. distance of adjacent PDMS microposts remaining constant over the whole stretching period.

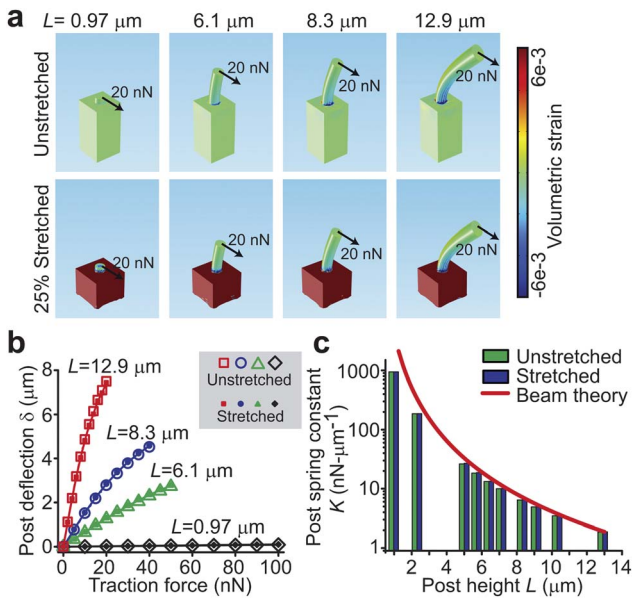

Fig. 3 Numerical analysis of mechanics of the PDMS micropost on the mPAM using the finite-element method (FEM). (**a**) Graphical depiction of FEM analysis of the PDMS microposts of different heights (L) each bending in response to an applied horizontal traction force (F) of 20 nN, with the underlying PDMS base membranes unstretched (*top panel*) or equibiaxially stretched (*bottom panel*; 25%). Color scale indicates volumetric strain (unitless). (**b**) Deflection δ of the top surface of the micropost plotted as a function of traction force F, as calculated by FEM analysis, for PDMS microposts of different lengths and on both unstretched (*large open symbols*) and equibiaxially stretched (*small solid symbols*; 25% stretch) mPAMs. (**c**) Nominal spring constant (K) of the PDMS microposts as a function of L, as computed from FEM analysis (bars; *green* for microposts on unstretched mPAMs and *blue* for microposts on stretched ones) and from the *Euler-Bernoulli* beam theory (*red* curve).

PDMS microposts under a horizontal force F of 20 nN, for both unstretched (top row) and 25% stretched (bottom row) mPAMs. Strain in the PDMS base membrane remained largely isolated and did not propagate towards the PDMS micropost tops. Strain at the top surface of the PDMS micropost was essentially zero for either unstretched or stretched mPAMs, regardless of the micropost height L, consistent with our experimental observation in Fig. 2a&c. We further calculated the nominal spring constant K of the PDMS microposts for both unstretched and stretched mPAMs, by determining their force (F)-displacement (δ) curves and then linearly extrapolating F to zero post deflection δ, where $K = dF/d\delta$ ($\delta \rightarrow 0$) (Fig. 3b).[15] Our numerical calculations suggested that K varied within 2% of each other for microposts on unstretched and 25% stretched mPAMs. Thus, we concluded that neither geometry of the PDMS micropost nor its spring constant K (and therefore rigidity) was affected by stretch of the mPAM.

To study the dynamic contractile response of VSMCs to cell stretch, we sparsely plated single VSMCs on a mPAM with the PDMS micropost height L of 8.3 μm. This micropost height was chosen to mimic the mechanical stiffness of vascular smooth muscle tissue *in vivo* (1–5 kPa).[6,26] Prior to stretch of the mPAM, each single live VSMC was monitored for 5 min to obtain their baseline contractility (F_{ini}) (Fig. 4a). At the onset of stretch (defined as $T_{ini} = 5$ min), a rapid step increase of static mPAM stretch (either 6% or 15%) was applied to VSMCs and was held constant for another 60 min (defined as $T_{final} = 65$ min), with the temporal evolution of the VSMC contractile response continuously monitored. This period of 60 min was chosen to allow sufficient time for VSMCs to respond to a sustained cell stretch.

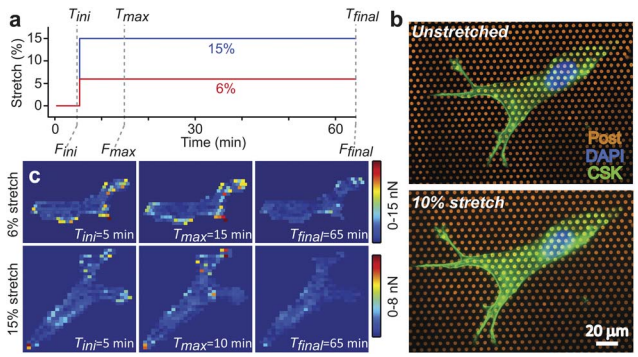

Fig. 4 Temporal progression of mPAM stretch and single-cell observation. (**a**) Schematic showing temporal regulation of static mPAM stretch. Each single live VSMC was continuously monitored for 5 min prior to mPAM stretch to obtain their baseline contractility F_{ini}. At the onset of stretch when $T_{ini} = 5$ min, a rapid step increase of static mPAM stretch (either 6% or 15%) was applied to the cell, and the static mPAM stretch was held constant for another 60 min ($T_{final} = 65$ min). T_{max} indicates the time point when the cell could reach its maximum reactive contractility of F_{max}. F_{final} indicates the cell contractile force at $T_{final} = 65$ min. (**b**) Representative fluorescence images showing single VSMCs on unstretched (*top*) and 10% stretched (*bottom*) mPAMs. VSMCs were stained with DAPI, fluorophore-labeled phalloidin and DiI to visualize nuclei, actin filaments, and underlying PDMS posts, respectively. (**c**) Colorimetric maps showing subcellular contractile force distributions for single VSMCs at T_{ini}, T_{max}, and T_{final} during 6% (*top panel*) and 15% (*bottom panel*) static mPAM stretches.

Single live VSMCs were stretched only once and then discarded, to avoid any experimental inconsistency due to possible adaptation of VSMCs to multiple stretch cycles.[55] The c.t.c. distance S of undeflected PDMS microposts (not attached to the cells) was monitored before and during the course of the mPAM stretch to confirm the stretch magnitude. As expected, right after the onset of the mPAM stretch, VSMCs enlarged accordingly with the increased c.t.c. distance of the PDMS microposts to which the cells were attached. Fig. 4b shows representative fluorescence images of an immunostained VSMC before and after stretch of the mPAM. Using the PDMS microposts as live-cell force sensors,[51–53] the subcellular contractile response of VSMCs to cell stretch was continuously monitored until the end of the stretch assay (Fig. 4c).

Using the mPAM, we observed that the direct physical effect of cell stretch could elicit both acute strengthening and slow adaptive behaviors in VSMC contractility. Following a single rapid step change of the mPAM static stretch, VSMCs rapidly increased their total contractility from F_{ini} and reached their maximum reactive contractility F_{max} at time T_{max} (the "stiffening phase"). This stiffening phase of VSMC contractility was followed by a gradual, monotonic decrease of VSMC contractility until the end of the stretch assay (the "softening phase"). During the stiffening phase for the 6% mPAM stretch, we observed a relative increase of VSMC contractility, calculated as $(F_{max} - F_{ini})/F_{ini} \times 100\%$, by 65.6 ± 13.4% within the first 19 ± 4.0 min after the onset of the mPAM stretch ($n = 8$) (Fig. 5a; the temporal evolution of the absolute total contractile response for individual cells is shown in Fig. S1a†). During the softening phase of the 6% mPAM stretch, a 49.8 ± 12.2% relative decrease of VSMC contractility below F_{max} (calculated as $(F_{max} - F_{final})/F_{max} \times 100\%$) was observed at $T_{final} = 65$ min. Both the stiffening and softening phases of the 6% cell stretch resulted in significant changes in the total contractility of VSMCs (Fig. 5a and Fig. S1a†). A 15% cell stretch using the mPAM elicited a similar biphasic contractile response in VSMCs ($n = 6$), in which the VSMC contractility increased 16.3 ± 3.8% in the first 8.2 ± 2.0 min after the onset of stretch, followed by a decrease of the VSMC contractility by 37.1 ± 7.4% below F_{max} at $T_{final} = 65$ min (Fig. 5b; the temporal evolution of the absolute total contractile response for individual cells is shown in Fig. S1b†). Both stiffening and softening phases for the 15% cell stretch showed significant changes in the total contractility of VSMCs (Fig. 5b and Fig. S1b†).

The relative increase of VSMC contractility during the stiffening phase was significantly different between the 6% and 15% mPAM stretches, with the 6% stretch resulting in a stronger increase of VSMC contractility than the 15% one (Fig. 5c). The time needed for VSMCs to reach their maximum reactive contractility and the relative decrease of VSMC contractility during the softening phase between the 6% and 15% cell stretches were also different, even though not statistically significant (Fig. 5d&e). Together, our observations here suggested that the biphasic contractile response was a general reaction of VSMCs to a sustained static cell stretch, and this biphasic contractile response of VSMCs appeared to be independent of the stretch magnitude.

One unique advantage of the mPAM over conventional continuous stretchable membranes was that the measured

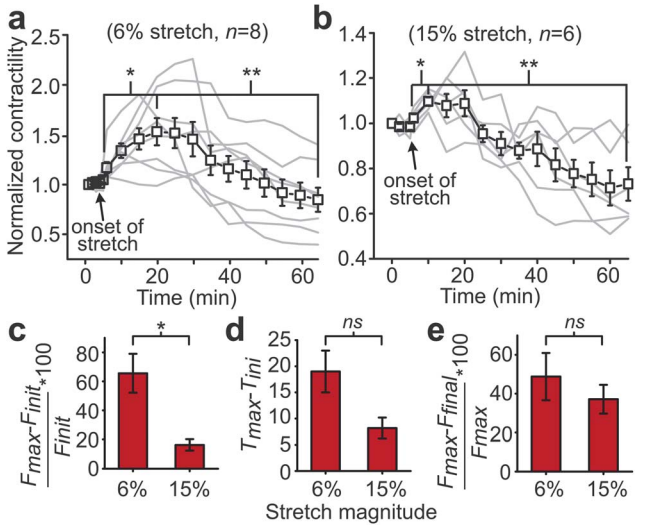

Fig. 5 Real-time live-cell contractile response of single VSMCs to static mPAM stretch. (**a&b**) Evolution of cellular contractility (normalized to baseline contractility prior to stretch) for individual cells (*gray* lines) and population means (*black* lines with marker symbols) under different stretch conditions as indicated (**a**: 6% stretch; **b**: 15% stretch). Cellular contractility of all cells was followed at 5 min intervals for the whole period of stretch assays. Each cell was exposed to the mPAM stretch once to avoid their potential adaptive response to multiple stretches. Error bars indicate ± standard errors (SE) of the cell populations. *P*-values calculated using the paired student's *t*-test are indicated for statistically significant differences ($P < 0.05$ (*) and $P < 0.005$ (**)). (**c**) Bar graph showing the relative maximum increase of cellular contractility, calculated as $(F_{max} - F_{ini})/F_{ini} \times 100$ (%), as a function of stretch magnitude. (**d**) Bar graph showing the time needed for individual VSMCs to reach their maximum reactive contractile forces after the onset of the mPAM stretch, or $T_{max} - T_{ini}$, as a function of stretch magnitude. *ns*, statistically not significant. (**e**) Bar graph showing the relative decrease of cellular contractility from T_{max} to T_{final}, calculated as $(F_{max} - F_{final})/F_{max} \times 100$, as a function of stretch magnitude.

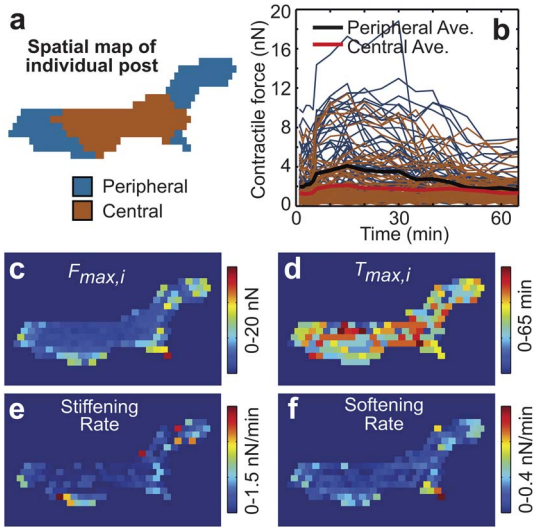

Fig. 6 Subcellular analysis of the biphasic contractile response of single VSMCs to the 6% static mPAM stretch. (**a**) Spatial map of the individual PDMS microposts underneath the VSMC. The microposts were labeled with different colors to indicate their distances from the cell's geometric centroid (*blue*: microposts at the cell periphery; *gold*: microposts in the cell's central region). (**b**) Evolution of contractile forces exerted on the individual PDMS microposts underneath the VSMC tracked throughout the whole stretch assay. *Blue* curves were from PDMS microposts at the cell periphery and *gold* curves were from the PDMS microposts at the central region of the cell. The bold black curve corresponds to the peripheral population mean and the bold red line corresponds to the central population mean. (**c**) Colorimetric map showing the spatial distribution and magnitude of the maximum reactive contractile forces exerted on the hexagonally arranged PDMS microposts ($F_{max,i}$) developed during the whole stretch assay. (**d**) Colorimetric map showing the spatial distribution and magnitude of the time required for individual PDMS microposts ($T_{max,i}$) to reach $F_{max,i}$. (**e&f**) Colorimetric map showing the spatial distribution of increasing (**e**) and decreasing (**f**) rates of reactive contractile forces for individual PDMS microposts during the stiffening and softening phases, respectively. Increasing rate of reactive contractile forces during the stiffening phase was defined as $(F_{max,i} - F_{ini,i})/(T_{max,i} - T_{ini})$, while decreasing rate of reactive contractile forces during the softening phase as $(F_{max,i} - F_{final,i})/(T_{final} - T_{max,i})$.

subcellular contractile forces of VSMCs could be attributed directly to individual FAs on the PDMS micropost tops.[15] This enabled us to track the temporal evolutions of subcellular contractile forces exerted on individual FAs throughout the entire stretch assays. For these subcellular analyses, individual PDMS microposts underneath single VSMCs were first evenly divided into two groups based on their relative distances from the cell's geometric centroid (central *vs.* peripheral microposts) (Fig. 6a). We observed that prior to the 6% mPAM stretch, contractile forces exerted on FAs were not uniform across single VSMCs, with contractile forces exerted on peripheral FAs noticeably higher than those exerted on central ones (Fig. 4c).[15] This anisotropic distribution of contractile forces was largely retained during the course of the static mPAM stretch (Fig. 4c). From the temporal evolutions of contractile forces exerted on each individual FA, we noticed that contractile responses of individual FAs to cell stretch were rather heterogeneous and covered a wide spectrum of different behaviors (Fig. 6b). Specifically, we observed that each individual FA could generate a unique contractile response, reaching the maximum reactive contractile force (defined as $F_{max,i}$) at a different time point (defined as $T_{max,i}$) during the course of cell stretch. In the stiffening phase, increases of CSK contractile forces exerted on peripheral FAs were generally greater than those for central FAs, while in the softening phase peripheral FAs tended to decrease their contractility more rapidly than the central FAs (Fig. 6b and Fig. S2a–c†). Averages of the contractile forces exerted on individual FAs in peripheral and central cellular regions tended to follow the average trend of the whole-cell total contractile response (Fig. S2a–c†). We further plotted colorimetric maps to show spatial distributions and magnitudes of $F_{max,i}$ and $T_{max,i}$ across the whole VSMC under the 6% static cell stretch, which revealed clearly that the reactive VSMC contractility was mainly contributed from FAs on the cell periphery initially bearing greater contractile stresses (Fig. 6c), and that central FAs subjected to less contractile forces prior to cell stretch took longer time to reach their $F_{max,i}$ after cell stretch (Fig. 6d). We further calculated rates of contractile force changes for each individual FA in both the stiffening (defined as $(F_{max,i} - F_{ini,i})/(T_{max,i} - T_{ini,i})$, or the stiffening rate) and softening phases (defined as

$(F_{max,i} - F_{final,i})/(T_{final,i} - T_{max,i})$, or the softening rate). Fig. 6e&f plotted the stiffening and softening rates of individual FAs for the 6% static cell stretch as colorimetric maps, from which it was clear that both the stiffening and softening rates of FAs were rather heterogeneous across individual VSMCs and the dynamic changes of FAs and their contractile forces were mainly concentrated on the cell periphery. Identical calculations were performed for other VSMCs subjected to 6% cell stretch ($n = 8$), and we had obtained similar results (Fig. S2a–c & Fig. S3a–c†).

To determine the effect of stretch amplitude on the dynamic contractile responses of individual FAs of VSMCs, we performed a similar subcellular analysis for VSMCs subjected to the 15% mPAM stretch ($n = 6$) (Fig. 7, Fig. S2d–f & Fig. S3d–f†). All VSMCs analyzed showed comparable results to those stretched at 6%, with a representative cell shown in Fig. 7. A spatial map in Fig. 7a depicts how the cell was divided into peripheral and central regions. Fig. 7b plots the heterogeneous temporal evolutions of contractile forces exerted on individual FAs of the cell, with the average contractile forces for individual FAs in the peripheral and central regions included for comparison. Once again, for 15% cell stretch, the peripheral FAs contributed more significantly to the total contractility increase in the stiffening phase, while in the softening phase, contractile forces exerted on individual peripheral FAs decreased more rapidly (Fig. 7b, Fig. S2d–f & Fig. S3d–f†). Similar to Fig. 6c, the colorimetric map in Fig. 7c shows the spatial distribution of $F_{max,i}$ within the cell, where larger values of $F_{max,i}$ were distributed around the cell periphery. Similar to Fig. 6d, distribution of $T_{max,i}$ in Fig. 7d shows a distinct pattern, with the central FAs subjected to less contractile forces prior to the cell stretch taking a longer time to reach their $F_{max,i}$ after the mPAM stretch. The stiffening and softening rates of individual FAs for the 15% static mPAM stretch were plotted in Fig. 7e&f, from which it was clear that the dynamic changes of contractile forces on FAs were mainly concentrated on the cell periphery for the 15% cell stretch.

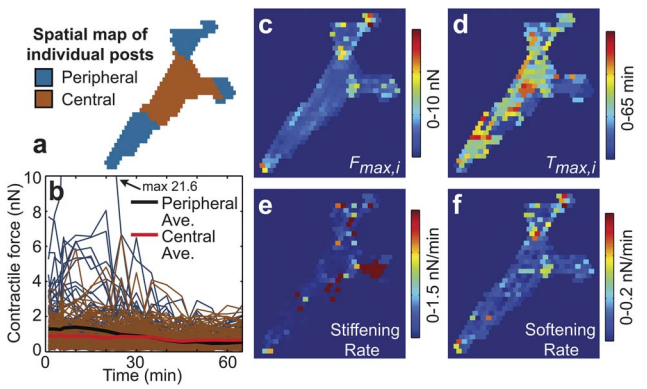

Fig. 7 Subcellular analysis of the biphasic contractile response of single VSMCs to the 15% static mPAM stretch. (**a**) Spatial map of the individual PDMS microposts underneath the VSMC. The microposts were labeled with different colors to indicate their distances to the cell periphery (*blue*: microposts at the cell periphery; *gold*: microposts in the cell's central region). (**b**) Evolution of contractile forces exerted on the individual PDMS microposts underneath the VSMC tracked throughout the whole stretch assay. *Blue* curves were from PDMS microposts at the cell periphery and *gold* curves were from the PDMS microposts at the center region of the cell. The bold black curve corresponds to the peripheral population mean and the bold red line corresponds to the central population mean. The numerical data in the plot indicates the maximum value that the outlier curves reached outside the plot window. (**c**) Colorimetric map showing the spatial distribution and magnitude of the maximum reactive contractile forces exerted on the hexagonally arranged PDMS microposts ($F_{max,i}$) developed during the whole stretch assay. (**d**) Colorimetric map showing the spatial distribution and magnitude of the time required for individual PDMS microposts ($T_{max,i}$) to reach $F_{max,i}$. (**e&f**) Colorimetric map showing the spatial distribution of increasing (**e**) and decreasing (**f**) rates of reactive contractile forces for individual PDMS microposts during the stiffening and softening phases, respectively. Increasing rate of reactive contractile forces during the stiffening phase was defined as $(F_{max,i} - F_{ini,i})/(T_{max,i} - T_{ini})$, while decreasing rate of reactive contractile forces during the softening phase as $(F_{max,i} - F_{final,i})/(T_{final} - T_{max,i})$.

In this present work, we designed and implemented the mPAM system that allowed for quantitative control and real-time measurements of mechanical stimuli and subcellular biomechanical responses. Using the mPAM, we achieved a detailed live-cell subcellular analysis of the contractile response of VSMCs to cell stretch at the single FA level. Incorporation of the PDMS micropost array onto the stretchable PDMS base membrane to generate the mPAM offered several advantages over conventional continuous membranes for cell stretch. First, the PDMS microposts can serve simultaneously as independent and highly sensitive contractile force sensors to report live-cell contractile responses at at the single FA level. This represents a significant strength for biomechanics studies where a measurement of the cellular contractile response to cell stretch is desirable. Second, the regularly arranged PDMS microposts can be used automatically as high-precision fiducial markers to gauge the magnitude of cell stretch, eliminating the necessary step for continuous membranes to mark their surfaces for assessments of the stretch magnitude.[29,56,57] Third, the geometry of the PDMS micropost can be precisely controlled to regulate substrate rigidity and adhesive ECM pattern independently of effects on other surface properties.[15,51–54] Thus, the mPAM system can serve as a new class of the synthetic biointerfacial system. Cell stretch, substrate rigidity, adhesive ECM pattern, and surface chemistry and topography can be independently controlled to facilitate characterization and study of complex biointerfacial cellular phenomena.

Using the mPAM, we showed that a sustained static cell stretch could elicit a biphasic behavior in VSMC contractility: VSMCs first increased contraction ("stiffening") before they gradually released contractility ("softening"). This biphasic response of VSMC contractility suggested that VSMCs could acutely contract to resist rapid cell deformation, and they could also allow slow adaptive inelastic CSK reorganization in response to a sustained cell stretch. Interestingly, we also observed that the magnitude of cell stretch could have a differential effect on the dynamic biphasic response of VSMC contractility: compared to the 6% static mPAM stretch, the 15% one resulted in a shortened stiffening phase with a limited enhancement in contractility as well as an exacerbated softening phase with much decreased contractility. A detailed subcellular analysis revealed that the reactive VSMC contractility in both the stiffening and softening phases was heterogeneous, and the reactive VSMC contractility was mainly

contributed from FAs on the cell periphery initially bearing greater contractile stresses. The FAs that did not experience evident changes in contractility in the stiffening phase appeared to have initial contractile forces less than 2 nN, and these FAs were mostly located in the central region of the cell (Fig. 6&7). Together, these observations raised the interesting possibility that a minimum level of initial FA stress (about 2 nN) might be required to sensitize mechanosensation by FAs, and the external and reactive contractile forces might be cooperatively involved in regulating FA signaling and downstream biomechanical responses of VSMCs.

From our observations, it is tempting to speculate that the initial FA stress, which regulates the molecular complexity and organization of FAs, is capable of modulating the molecular FA sensitivity, and thus local CSK responses, to cell stretch. The molecular composition of FAs has been previously shown to regulate local CSK contractility, and though the exact molecular mechanism is largely unknown, several key FA proteins (including talin, vinculin, and zyxin) have been implicated for the regulation of CSK contractility.[58–60] For example, the force-mediated dynamics of FAs and the CSK have been recently demonstrated using a biosensor that reported the tension across vinculin.[60] It has shown that mechanosensitive vinculin is under a high tension in FAs that will assemble and strengthen, whereas it is under a low tension in FAs that will disassemble under the cellular contractile forces. The force-dependent mechanosensitivity of FA proteins (in this case, vinculin) is consistent with what we observed in stretching VSMCs using the mPAM. The spatial specificity and heterogeneity of dynamic FA and contractile responses has also been observed in single migrating cells,[61] where FA strengthening is restricted to the front of the migrating cells, even though the underlying mechanism for this spatial specificity of dynamic FA and contractile responses is largely unknown.[5]

The biphasic contractile response of VSMCs to the static mPAM stretch was somewhat unexpected, as previous studies have only reported either reinforcement of FAs (indicated by a continuous increase in CSK contractility exerted on the FAs) or fluidization of the CSK (shown as a decrease in CSK contractility exerted on the FAs) upon application of the cell stretching forces.[28,36,62–65] The molecular mechanism that regulates whether FAs and CSK structures strengthen or disassemble under forces are not yet clear, and likely the observed biphasic VSMC contractile response resulted from competitive intracellular mechanisms triggering both reinforcement and disassembly of FA proteins.[3,5] The rapidly applied mPAM stretch may have first resulted in conformational changes in FA proteins that induce protein recruitments to reinforce FAs and their mechanical linkages to the local CSK structure, thus increasing contractile forces exerted on the FAs. After the contractile forces reach a maximum threshold level, linker FA proteins may start to increase their dissociation from the attached integrin or actin filaments, leading to a shortened adhesion lifetime and thus a decreased contractile stress. This largely speculated dynamic molecular picture for force-mediated FA regulation can also explain the differential effect of the stretch magnitude on the biphasic response of VSMC contractility between the 6% and 15% static cell stretches, as the rapid increase of the cell strain for the 15% cell stretch may have caused FAs to reach their maximum contractile threshold at an earlier time point to trigger FA dissociation. Future investigations using live-cell imaging with fluorescence-tagged FA proteins will help elucidate the molecular details of FA reinforcement and dissociation in regulating contractile responses of VSMCs.

Very recently, Nagayama *et al.* have developed a stepper motor-controlled uniaxial cell stretch system with the PDMS micropost array adhered to a rectangular PDMS stretching compartment.[32] Even though their system shares some functional similarity to the mPAM reported here, Nagayama *et al.* have only examined the effect of uniaxial stretch on VSMC contractility using a roughly triangular waveform of cell stretch. The cell stretch protocol used in our work differed significantly from theirs, making direct comparisons of the CSK contractility results difficult. Nonetheless, similar to the results reported here, Nagayama *et al.* have observed heterogeneous contractile responses of individual FAs from single VSMCs. Taken together, the results reported here as well as by Nagayama *et al.* clearly demonstrate the unique advantages of incorporating the PDMS micropost array into the conventional cell stretch assays to report live-cell subcellular contractile responses at the single FA level.

Conclusions

In summary, here we reported a microengineered cell stretching device to obtain real-time live-cell quantitative measurements of the contractile response of single VSMCs to cell stretch at the level of single FAs. We observed that the contractile response of VSMCs to sustained static cell stretch was biphasic, with VSMCs first increasing their contraction ("stiffening") before gradually releasing their contractility ("softening"). The contractile response of VSMCs was spatially inhomogeneous and force-dependent, as the responsive FAs contributing to the contractile response were mainly concentrated on the cell periphery and were initially bearing greater contractile stresses. This spatial specificity and force-dependence of dynamic FA and CSK contractile responses are not understood yet, but likely involve the varying strengths and dynamic characteristics of the force-bearing subcellular structures (such as individual adhesion proteins and the local CSK structures) that could regulate distinct signaling pathways and downstream cellular behaviors such as the contractile behaviors of VSMCs.

Materials and methods

Fabrication of micropost array membranes (mPAMs)

Elastomeric micropost array membranes (mPAMs) were generated using previously described PDMS micropost arrays in addition to the techniques described here.[15,54] First, the negative mold for the PDMS micropost array was prepared using 1 : 10 (w:w, curing agent:base) ratio poly-(dimethylsiloxane) (PDMS; Sylgard 184, Dow-Corning, Midland, MI) prepolymer. PDMS prepolymer was degassed and poured over the silicon micropost array master and baked for 20 min at 110 °C. Cured PDMS polymer was peeled off from the silicon master and oxidized with the air plasma (Plasma Prep II, West Chester, PA) for 1 min. The negative PDMS mold was then silanized with

(tridecafluoro-1,1,2,2,-tetrahydrooctyl)-1-trichlorosilane vapor (United Chemical Technologies, Bristol, PA) overnight under vacuum. Round coverslips of a diameter of 18 mm and a thickness of 220 μm were prepared in parallel by silanization for 10 min. 1 : 10 PDMS prepolymer was then spin-coated onto the silanized coverslips at 2,000 rpm for 30 s to produce a thin PDMS prepolymer film of 40 μm thick. These coverslips were then baked for 20 min at 110 °C. To generate the PDMS micropost array on the coverslip, a small amount of 1 : 10 PDMS prepolymer was placed on the negative PDMS mold and the coverslip was pressed upside down on top of the negative mold. The whole assembly was baked at 110 °C for 20 h, before the PDMS negative mold was carefully peeled away from the coverslip. The coverslip with the PDMS micropost array was placed in 100% ethanol and sonicated for 1 min to restore collapsed posts before dry release with liquid CO_2 (Samdri-PVT-3D, Tousimis, Rockville, MD).

To generate the PDMS base membrane, 1 : 10 PDMS prepolymer was spin-coated onto the lid of the 100 mm Petri dish (BD Falcon, Franklin Lakes, NJ) at 500 rpm to achieve a PDMS layer 100 μm thick. The Petri dish lid was then baked at 60 °C for 1.5 h. The mPAM was assembled from the PDMS micropost array on the coverslip and the PDMS base membrane on the lid of the Petri dish. First, all excess PDMS on the coverslip was trimmed away to leave only the area covered with the PDMS microposts. Using a needle-nose tweezer, the PDMS micropost array was removed from the coverslip, turned upside down and placed onto a holder, and plasma treated together with the PDMS base membrane (still on the Petri dish) for 45 s. The PDMS micropost array was immediately flipped over onto the PDMS base membrane to allow PDMS-PDMS bonding to occur, and then the final mPAM assembly was baked for an additional 20 min at 60 °C.

Finite element method (FEM) analysis of nominal spring constant of PDMS microposts under stretch conditions

FEM analysis was performed using COMSOL, a commercially-available FEM program (COMSOL, Inc., Burlington, MA), to analyze defections of the PDMS micropost under different horizontal traction forces. Our FEM model consisted of a cylindrical PDMS micropost (with a diameter D of 1.83 μm and a height L of 0.97–12.9 μm) placed atop a 5 × 5 × 10 μm rectangular prism (Fig. 3a). The whole assembly was modeled as neohookian hyperelastic with a modulus of elasticity E of 2.5 MPa and was discretized into fine tetrahedral mesh elements calibrated for general physics in COMSOL. For unstretched conditions, the bottom and four sides of the rectangular prism were assigned fixed boundary conditions, while in stretched conditions, the prism bottom was constrained and the four side faces were prescribed by a displacement that would reproduce a 25% stretch for the PDMS base membrane. A horizontal traction force F was then applied uniformly at all of the nodes on the top surface of the PDMS micropost. FEM analysis was performed to determine the displacement δ of the center node on the micropost top surface due to F. From the force-displacement curve (Fig. 3b), the nominal spring constant K of the PDMS micropost can be determined by linearly extrapolating F to zero post deflection δ, and then computing $K = dF/d\delta$ ($\delta \rightarrow 0$).

Cell culture and reagents

Vascular smooth muscle cells (VSMCs, CC-2583, Lonza, Walkersville, MD) were cultured in the Smooth Muscle Cell Basal Medium (SmBM) with SmGM-2 SingleQuots (CC-4149, Lonza). Cell passaging was performed using the Clonetics ReagentPack reagents (CC-5034, Lonza). Only early passages of VSMCs were used for experiments (passage 3–4). The same cell medium was used for imaging as was used for cell growth.

Surface functionalization of the mPAM and assembly of the mPAM and CSD

Microcontact printing was applied to functionalize the top surface of the PDMS micropost array on the mPAM.[51] Briefly, a flat PDMS stamp was coated with 50 μg mL^{-1} fibronectin (BD Biosciences, San Jose, CA) in distilled (DI) water for 1 h, and then blown dry with nitrogen. The fibronectin-coated stamp was placed in contact with the plasma treated, surface-oxidized PDMS micropost array on the mPAM. The stamp was left in contact with the microposts for 15 s to transfer fibronectin from the stamp to the PDMS microposts. The PDMS microposts were labeled by incubating with 5 μg mL^{-1} of Δ^9-DiI (Invitrogen, Carlsbad, CA) in DI water at room temperature for 1 h. Following microcontact printing, protein adsorption to all PDMS surfaces not coated with fibronectin was prevented by incubating in 0.1–1% Pluronics F127 NF (BASF, Ludwigshafen, Germany) in DI water for 30 min at room temperature. VSMCs were then sparsely seeded onto the PDMS micropost array and then allowed to attach and spread out for 48 h before observation. The mPAM was transferred to the polycarbonate cell stretching device (CSD), and the whole assembly was then placed into a 60 mm glass bottom culture dish (MatTek Corporation, Ashland, MA) with a round 25 mm diameter, 150 μm thickness coverslip glued in the bottom, filled with 2–3 mL cell media. The CSD-culture dish assembly was kept in the cell incubator for 1 h before the mPAM stretch assays using live-cell fluorescence microscopy.

Cellular contractile force quantification

During equibiaxial mPAM stretch assays, the PDMS micropost array was imaged using a monochrome charge-coupled device (CCD) camera (AxioCam, Carl Zeiss MicroImaging, Thornwood, NY) attached to an inverted microscope (Zeiss Axio Observer Z1, Carl Zeiss MicroImaging) with 40 × EC Plan-Neofluar objective (0.75 Ph2 D = 0.71 M27, Carl Zeiss MicroImaging). The microscope was enclosed in an environmental incubator (XL S1 incubator, Carl Zeiss MicroImaging) to maintain the experimental environment at 37 °C and 5% CO_2. For each cell, fluorescence images of the Δ^9-DiI-stained PDMS microposts were acquired by focusing on a plane intersecting the micropost array tips. Baseline traction force was recorded at 1 frame per min for 5 min before activating the vacuum system (DigiVac Model 450, DigiVac, Matawan, NJ) to equibiaxially stretch the mPAM and thus the cells attached on the PDMS micropost array. A constant static mPAM stretch was maintained for 60 min, with images recorded at 5 min intervals. Cells were considered viable if they remained attached to the PDMS

microposts for the duration of the experiment and did not round up or detach.

Each fluorescence image was analyzed using a customized MATLAB program (Mathworks) to compute traction forces.[54] A previously described localized thresholding algorithm (LT) was used to determine the centroid of each post. A selected region of the image was converted to black and white, where the sum of white pixels representing the expected size of the post cross-sectional area was determined with thresholding. A 2D *Gaussian* fit was used to model the grayscale intensity profile of the PDMS post and determined the centroid by nonlinear least squares fit. This step determined the deflected positions of the microposts, and the deflected positions were compared against a regular grid, aligned using undeflected "free" microposts as reference points. The deflection δ for the "attached" posts was converted to horizontal traction force vectors using classical beam theory with a point force, and $F = K \times \delta$, where K was the nominal spring constant determined through FEM simulations (See Fig. 3).

The total contractility of individual cells was calculated as the sum of the magnitudes of the contractile forces exerted on all the attached PDMS microposts. We characterized the noise level of the displacement of the unattached free PDMS micropost to be about 0.05 nN. Thus, any PDMS micropost with $F < 0.05$ nN were considered unattached. Peripheral and central regions of the cell were determined from the cell's geometric centroid. First, the geometric centroid of the cell was calculated using the undeflected locations of the attached PDMS microposts as coordinates. Then, in a constant radius originating at the centroid, half of the total number of the attached PDMS microposts were considered "central" and the remaining half were "peripheral" (see Fig. 6a & Fig. 7a).

Cell staining

Cells were fixed and stained for representative stretching images while the membrane was attached to the CSD. VSMCs were fixed in 4% paraformaldehyde (Electron Microscopy Science, Hatfield, PA) in PBS and stained for phalloidin using Alexa Fluor 647 (A22287, Invitrogen, Carlsbad, CA) and DAPI (D21490, Invitrogen, Carlsbad, CA).

Acknowledgements

We acknowledge financial support from the National Science Foundation (NSF CMMI 1129611) and the department of Mechanical Engineering at the University of Michigan, Ann Arbor. We thank P. Mao for his assistance in microfabrication of the silicon micropost array master. We thank M. Yang and C. Chen for sharing with us the MATLAB program to quantify cellular contractile forces. We acknowledge valuable comments and suggestions on the manuscript by K. Garikipati and G.A. Meininger. The Massachusetts Institute Technology (M.I.T.) Microsystems Technology Laboratories (MTL) is acknowledged for support in microfabrication.

References

1 B. Geiger, A. Bershadsky, R. Pankov and K. M. Yamada, *Nat. Rev. Mol. Cell Biol.*, 2001, **2**, 793–805.
2 A. W. Orr, B. P. Helmke, B. R. Blackman and M. A. Schwartz, *Dev. Cell*, 2006, **10**, 11–20.
3 V. Vogel and M. Sheetz, *Nat. Rev. Mol. Cell Biol.*, 2006, **7**, 265–275.
4 B. Geiger, J. P. Spatz and A. D. Bershadsky, *Nat. Rev. Mol. Cell Biol.*, 2009, **10**, 21–33.
5 B. D. Hoffman, C. Grashoff and M. A. Schwartz, *Nature*, 2011, **475**, 316–323.
6 D. E. Discher, P. Janmey and Y. L. Wang, *Science*, 2005, **310**, 1139–1143.
7 M. A. Wozniak and C. S. Chen, *Nat. Rev. Mol. Cell Biol.*, 2009, **10**, 34–43.
8 C.-M. Lo, H.-B. Wang, M. Dembo and Y.-l. Wang, *Biophys. J.*, 2000, **79**, 144–152.
9 M. J. Paszek, N. Zahir, K. R. Johnson, J. N. Lakins, G. I. Rozenberg, A. Gefen, C. A. Reinhart-King, S. S. Margulies, M. Dembo, D. Boettiger, D. A. Hammer and V. M. Weaver, *Cancer Cell*, 2005, **8**, 241–254.
10 A. J. Engler, S. Sen, H. L. Sweeney and D. E. Discher, *Cell*, 2006, **126**, 677–689.
11 P. M. Gilbert, K. L. Havenstrite, K. E. G. Magnusson, A. Sacco, N. A. Leonardi, P. Kraft, N. K. Nguyen, S. Thrun, M. P. Lutolf and H. M. Blau, *Science*, 2010, **329**, 1078–1081.
12 S. Peyton, C. Ghajar, C. Khatiwala and A. Putnam, *Cell Biochem. Biophys.*, 2007, **47**, 300–320.
13 C. S. Chen, *J. Cell Sci.*, 2008, **121**, 3285–3292.
14 T. Yeung, P. C. Georges, L. A. Flanagan, B. Marg, M. Ortiz, M. Funaki, N. Zahir, W. Ming, V. Weaver and P. A. Janmey, *Cell Motil. Cytoskeleton*, 2005, **60**, 24–34.
15 J. Fu, Y.-K. Wang, M. T. Yang, R. A. Desai, X. Yu, Z. Liu and C. S. Chen, *Nat. Methods*, 2010, **7**, 733–736.
16 P. F. Davies, *Physiological Reviews*, 1995, **75**, 519–560.
17 D. E. Ingber, *Ann. Med.*, 2003, **35**, 564–577.
18 C. Hahn and M. A. Schwartz, *Nat. Rev. Mol. Cell Biol.*, 2009, **10**, 53–62.
19 H. D. Intengan and E. L. Schiffrin, *Hypertension*, 2001, **38**, 581–587.
20 S. Schwartz, R. Geary and L. Adams, *Curr. Atheroscler. Rep.*, 2003, **5**, 201–207.
21 R. M. K. W. Lee, S. L. Sandow and J. G. R. DeMey, *Physiology*, 2009, **24**, 271–272.
22 G. Osol, *Journal of Vascular Research*, 1995, **32**, 275–292.
23 M. J. Davis and M. A. Hill, *Physiological Reviews*, 1999, **79**, 387–423.
24 S. Suresh, *Acta Mater.*, 2007, **55**, 3989–4014.
25 K. J. Van Vliet, G. Bao and S. Suresh, *Acta Mater.*, 2003, **51**, 5881–5905.
26 G. Bao and S. Suresh, *Nat. Mater.*, 2003, **2**, 715–725.
27 T. D. Brown, *J. Biomech.*, 2000, **33**, 3–14.
28 X. Trepat, L. Deng, S. S. An, D. Navajas, D. J. Tschumperlin, W. T. Gerthoffer, J. P. Butler and J. J. Fredberg, *Nature*, 2007, **447**, 592–595.
29 N. Gavara, P. Roca-Cusachs, R. Sunyer, R. Farré and D. Navajas, *Biophys. J.*, 2008, **95**, 464–471.
30 S. Lehoux, B. Esposito, R. Merval and A. Tedgui, *Circulation*, 2005, **111**, 643–649.
31 S. Na, A. Trache, J. Trzeciakowski, Z. Sun, G. Meininger and J. Humphrey, *Ann. Biomed. Eng.*, 2008, **36**, 369–380.
32 K. Nagayama, A. Adachi and T. Matsumoto, *J. Biomech.*, 2011, **44**, 2699–2705.
33 G. W. Schmid-Schönbein, K. L. Sung, H. Tözeren, R. Skalak and S. Chien, *Biophys. J.*, 1981, **36**, 243–256.
34 E. Evans and A. Yeung, *Biophys. J.*, 1989, **56**, 151–160.
35 W. H. Goldmann, *Biotechnol. Lett.*, 2000, **22**, 431–435.
36 O. Thoumine and A. Ott, *Journal of Cell Science*, 1997, **110**, 2109–2116.
37 C. Rotsch and M. Radmacher, *Biophys. J.*, 2000, **78**, 520–535.
38 S. Kumar and J. H. Hoh, *Traffic*, 2001, **2**, 746–756.
39 S. C. Kuo and M. P. Sheetz, *Trends Cell Biol.*, 1992, **2**, 116–118.
40 P. A. Valberg and H. A. Feldman, *Biophys. J.*, 1987, **52**, 551–561.
41 M. Puig-De-Morales, M. Grabulosa, J. Alcaraz, J. Mullol, G. N. Maksym, J. J. Fredberg and D. Navajas, *Journal of Applied Physiology*, 2001, **91**, 1152–1159.
42 A. R. Bausch, F. Ziemann, A. A. Boulbitch, K. Jacobson and E. Sackmann, *Biophys. J.*, 1998, **75**, 2038–2049.
43 A. R. Bausch, W. Möller and E. Sackmann, *Biophys. J.*, 1999, **76**, 573–579.
44 F. J. Alenghat, B. Fabry, K. Y. Tsai, W. H. Goldmann and D. E. Ingber, *Biochem. Biophys. Res. Commun.*, 2000, **277**, 93–99.

45 B. D. Matthews, D. R. Overby, F. J. Alenghat, J. Karavitis, Y. Numaguchi, P. G. Allen and D. E. Ingber, *Biochem. Biophys. Res. Commun.*, 2004, **313**, 758–764.
46 F. Amblard, B. Yurke, A. Pargellis and S. Leibler, *Rev. Sci. Instrum.*, 1996, **67**, 818–827.
47 H. Huang, C. Y. Dong, H.-S. Kwon, J. D. Sutin, R. D. Kamm and P. T. C. So, *Biophys. J.*, 2002, **82**, 2211–2223.
48 B. G. Hosu, K. Jakab, P. Banki, F. I. Toth and G. Forgacs, *Rev. Sci. Instrum.*, 2003, **74**, 4158–4163.
49 N. J. Sniadecki, A. Anguelouch, M. T. Yang, C. M. Lamb, Z. Liu, S. B. Kirschner, Y. Liu, D. H. Reich and C. S. Chen, *Proc. Natl. Acad. Sci. U. S. A.*, 2007, **104**, 14553–14558.
50 S. R. Heidemann and D. Wirtz, *Trends Cell Biol.*, 2004, **14**, 160–166.
51 J. L. Tan, J. Tien, D. M. Pirone, D. S. Gray, K. Bhadriraju and C. S. Chen, *Proc. Natl. Acad. Sci. U. S. A.*, 2003, **100**, 1484–1489.
52 O. du Roure, *Proc. Natl. Acad. Sci. U. S. A.*, 2005, **102**, 2390–2395.
53 A. Saez, A. Buguin, P. Silberzan and B. Ladoux, *Biophys. J.*, 2005, **89**, L52–L54.
54 M. T. Yang, J. Fu, Y.-K. Wang, R. A. Desai and C. S. Chen, *Nat. Protoc.*, 2011, **6**, 187–213.
55 B. D. Matthews, D. R. Overby, R. Mannix and D. E. Ingber, *J. Cell Sci.*, 2006, **119**, 508–518.
56 W. W. Ahmed, M. H. Kural and T. A. Saif, *Acta Biomater.*, 2010, **6**, 2979–2990.
57 D. Wang, Y. Xie, B. Yuan, J. Xu, P. Gong and X. Jiang, *Integr. Biol.*, 2010, **2**, 288–293.
58 E. J. Cram, S. G. Clark and J. E. Schwarzbauer, *J. Cell Sci.*, 2003, **116**, 3871–3878.
59 M. Yoshigi, L. M. Hoffman, C. C. Jensen, H. J. Yost and M. C. Beckerle, *J. Cell Biol.*, 2005, **171**, 209–215.
60 C. Grashoff, B. D. Hoffman, M. D. Brenner, R. Zhou, M. Parsons, M. T. Yang, M. A. McLean, S. G. Sligar, C. S. Chen, T. Ha and M. A. Schwartz, *Nature*, 2010, **466**, 263–266.
61 C. E. Schmidt, A. F. Horwitz, D. A. Lauffenburger and M. P. Sheetz, *J. Cell Biol.*, 1993, **123**, 977–991.
62 N. Q. Balaban, U. S. Schwarz, D. Riveline, P. Goichberg, G. Tzur, I. Sabanay, D. Mahalu, S. Safran, A. Bershadsky, L. Addadi and B. Geiger, *Nat. Cell Biol.*, 2001, **3**, 466–472.
63 D. Riveline, E. Zamir, N. Q. Balaban, U. S. Schwarz, T. Ishizaki, S. Narumiya, Z. Kam, B. Geiger and A. D. Bershadsky, *J. Cell Biol.*, 2001, **153**, 1175–1186.
64 D. Choquet, D. P. Felsenfeld and M. P. Sheetz, *Cell*, 1997, **88**, 39–48.
65 R. Krishnan, C. Y. Park, Y.-C. Lin, J. Mead, R. T. Jaspers, X. Trepat, G. Lenormand, D. Tambe, A. V. Smolensky, A. H. Knoll, J. P. Butler and J. J. Fredberg, *PLoS One*, 2009, **4**, e5486.

